Restoration of Missing Data in Limited Angle Tomography Based on Helgason-Ludwig Consistency Conditions

Yixing Huang[1], **Xiaolin Huang**[1,2], **Oliver Taubmann**[1,3], **Yan Xia**[4], **Viktor Haase**[1,5], **Joachim Hornegger**[1,3], **Guenter Lauritsch**[5], **Andreas Maier**[1,3]

[1]Pattern Recognition Lab, Friedrich-Alexander-University Erlangen-Nuremberg, Erlangen, Germany

[2]Institute of Image Processing and Pattern Recognition, Shanghai Jiao Tong University, Shanghai, China

[3]Erlangen Graduate School in Advanced Optical Technologies, Erlangen, Germany

[4]Department of Radiology, Stanford University, USA

[5]Siemens Healthcare GmbH, Forchheim, Germany

E-mail: `yixing.yh.huang@fau.de`

April 2017

Abstract. In limited angle tomography, missing data in an insufficient angular scan will cause streak artifacts in the reconstructed images. Correspondingly, in the frequency domain representation of the imaged object, a double wedge-shaped region is missing. In this paper, we perform a regression in sinogram domain and an image fusion in frequency domain to restore the missing data. We first convert the sinogram restoration problem into a regression problem based on the Helgason-Ludwig consistency conditions. Due to its severe ill-posedness, regression only partially recovers the correct frequency components, especially lower frequency components, and will introduce erroneous ones, particularly higher frequencies. Bilateral filtering is utilized to retain the most prominent high frequency components and suppress erroneous ones. Afterwards, a fusion in the frequency domain utilizes the restored frequency components to fill the missing double wedge region. The proposed method is evaluated in a parallel-beam study on both numerical and clinical phantoms. The root-mean-square errors of the reconstructed images decrease from 302 HU to 78 HU for the noise-free Shepp-Logan phantom, from 355 HU to 175 HU for the noisy Shepp-Logan phantom, and from 187 HU to 56 HU for the clinical data. The results show that our method is promising in streak reduction and intensity offset compensation in both noise-free and noisy situations.

Keywords: limited angle tomography, Helgason-Ludwig consistency conditions, streak artifacts, regression, fusion

1. Introduction

In computed tomography (CT), a minimum angular range is required to acquire enough projection data for image reconstruction. However, in practical applications, the gantry rotation of a CT system might be restricted by other system parts or external obstacles. Reconstruction from data acquired with such an insufficient angular range is called limited angle tomography. The missing data will cause artifacts in the reconstructed image, typically in the form of streak artifacts.

The ill-posedness of the limited angle tomography problem has been well investigated and some stable approximate inversions are given. Davison and Louis (Davison 1983, Louis 1986) provided condition numbers for varying angular ranges by computing the singular value decomposition (SVD) of matrix representations of the Radon transform. Davison pointed out that mollification methods stabilize the inversion problem. Other stable approximate inversions can be obtained using the SVD pseudo-inverse or Tikhonov-Phillips regularization (Natterer 1986, Quinto 2006). Quinto (Quinto 2007) used microlocal analysis to predict which singularities (e.g., boundaries) of objects can be well reconstructed from limited angle data. Theoretically the Radon transform can detect a boundary point of an object when an X-ray tangent to the boundary at this point exists.

Iterative reconstruction algorithms can incorporate prior information to obtain a unique solution. For example, iterative projection onto convex sets (POCS) can be utilized to obtain high quality images (Saito & Kudo 1988, Olson 1995). Statistical prior information can also be incorporated into iterative reconstructions (Hanson & Wecksung 1983, Siltanen et al. 2003). Recently, iterative reconstruction algorithms with total variation (TV) regularization in particular (Sidky & Pan 2008, Ritschl et al. 2011, Wu et al. 2012, Frikel 2013), which exploits the sparsity at the image gradient domain, have become popular in limited angle tomography. As streaks in limited angle tomography are highly dependent on the scan trajectory, anisotropic total variation algorithms can be designed to reduce streaks more efficiently than isotropic ones (Chen et al. 2013, Huang et al. 2016). However, iterative algorithms require expensive computation. Deep learning with convolutional neural networks can learn compensation weights (Riess et al. 2013) for a mapping between limited angle data and artifact-free images while keeping the same computational complexity as a standard filtered backprojection (FBP) reconstruction (Würfl et al. 2016, Zhang et al. 2016).

To deal with data insufficiency problems, many extrapolation/interpolation methods have been proposed (Hsieh et al. 2004, Zamyatin & Nakanishi 2006, Constantino & Ozanyan 2008, Xia et al. 2015). They can improve the image quality for the truncation problem and the sparse projection problem. However, they are not effective for limited angle tomography where a large amount of data is missing. The Gerchberg-Papoulis based extrapolation/interpolation algorithms (Happonen & Ruotsalainen 2005, Qu et al. 2008, Qu & Jiang 2009) have been demonstrated beneficial for improving the image quality of limited angle tomography. An alternative approach is to restore the missing projection data based on data consistency conditions. Many consistency conditions have been explored. For example, epipolar consistency in cone-beam CT (Debbeler et al. 2013, Aichert et al. 2015) and John's equation (Patch 2002) describe redundency in cone-beam projection data. The 2-D Fourier transform of a parallel-beam or fan-beam sinogram should contain a double wedge zero region (Edholm et al. 1986, Mazin & Pelc 2010). Truncated parallel-beam and fan-beam data exhibits a polynomial behavior after integration with certain weights (Clackdoyle & Desbat 2015). The Helgason-Ludwig consistency conditions (HLCC) (Ludwig 1966, Helgason 1980). Essentially, HLCC are necessary and sufficient for a transform to be a Radon transform (Deans 2007). Louis and Törnig reformulated the sinogram extrapolation/interpolation problem into a system of linear equations based on HLCC such that an approximate sinogram can be estimated (Louis & Törnig 1980, Louis 1981). Willsky and Prince proposed to restore the complete sinogram by solving an Euler-Lagrange partial derivative equation which integrates HLCC as a constraint (Willsky & Prince 1990). Kudo and Saito utilized POCS to incorporate HLCC for limited angle sinogram recovery, but their approach requires a prior sinogram (Kudo & Saito 1991). Patch stated that HLCC can indirectly improve image quality for the problem of bad detector channels (Patch 2001).

In this paper, we propose a regression and fusion method to restore the missing data in limited angle tomography: In sinogram domain, we convert the sinogram recovery problem into a regression problem based on HLCC, which allows us to analyze its ill-posedness conveniently. Due to the ill-posedness, regression only partially recovers the correct frequency components, mainly for lower frequencies, and will introduce erroneous ones, particularly for higher frequencies. To deal with ill-posedness, we propose to use Lasso regression based on the sparsity of the coefficients. Bilateral filtering is utilized to obtain the most prominent high frequency components and suppress erroneous ones. Afterwards, in the frequency domain we perform a fusion of the filtered image and the image reconstructed from the limited angle sinogram. The fusion makes the most of the original measured data and only uses the filtered image for unobserved frequency components. The proposed method is demonstrated in both numerical and clinical phantoms in noise-free and noisy situations.

2. Method and materials

2.1. Background

The parallel-beam sinogram of a 2-D object $f(x, y)$ is denoted by

$$p(s,\theta) = \int_{-\infty}^{\infty} f(s\cos\theta - t\sin\theta, s\sin\theta + t\cos\theta)\mathrm{d}t, \tag{1}$$

where θ is the rotation angle and s is the detector index. In practice, the spatially bounded object can be assumed to be supported on a unit disk centered at the origin, i.e., $-1 \leq s \leq 1$. We define the nth order moment curve as,

$$a_n(\theta) = \int_{-1}^{1} p(s,\theta)T_n(s)\mathrm{d}s, \tag{2}$$

where $T_n(s) = s^n$. The Fourier transform of the moment curve is,

$$b_{n,m} = \frac{1}{2\pi}\int_0^{2\pi} a_n(\theta)e^{-im\theta}\mathrm{d}\theta. \tag{3}$$

HLCC (Ludwig 1966, Helgason 1980) can be expressed as,

$$b_{n,m} = 0, \quad |m| > n \text{ or } n+m \text{ is odd.} \tag{4}$$

When $T_n(s)$ is replaced by orthogonal polynomials, e.g., Chebyshev polynomials, Legendre polynomials or Gegenbauer polynomials, $p(s,\theta)$ can be conveniently restored from $a_n(\theta)$. In this paper, we use the Chebyshev polynomial of the second kind (Lewitt 1983),

$$U_n(s) = \frac{\sin((n+1)\arccos(s))}{\sqrt{1-s^2}} = \frac{\sin((n+1)t)}{\sin t}, \text{ where } s = \cos t. \tag{5}$$

Two important properties are attributed to the Chebyshev transform in Eq. (2):

(i) $U_n(s)$ is a family of orthogonal polynomials at domain [-1, 1] with the scalar weight $W(s) = (1-s^2)^{1/2}$, i.e.,

$$\int_{-1}^{1} W(s)\cdot U_n(s)\cdot U_m(s)\mathrm{d}s = \begin{cases} 0, & n \neq m \\ \pi/2, & n = m. \end{cases} \tag{6}$$

Thus, an approximate sinogram can be restored by the inverse Chebyshev transform from the moment curves,

$$p_{n_r}(s,\theta) = \frac{2}{\pi}\sum_{n=0}^{n_r} a_n(\theta)(W(s)\cdot U_n(s)), \tag{7}$$

where n_r is the number of orders used. When $n_r \to \infty$, the sinogram is restored exactly.

(ii) The Fourier transform of $W(s)\cdot U_n(s)$ is computed as,

$$\begin{aligned} &\mathcal{F}(W(s)\cdot U_n(s))(w) \\ &= \int_{-1}^{1} \sqrt{1-s^2}\cdot \tfrac{\sin((n+1)\arccos(s))}{\sqrt{1-s^2}}\cdot e^{-iws}\mathrm{d}s \\ &= -\int_{-\pi}^{\pi} \sin t\cdot \tfrac{\sin((n+1)t)}{\sin t}\cdot e^{-iw\cos t}\cdot \sin t\mathrm{d}t \\ &= \int_0^{\pi} \cos((n+2)t)e^{-iw\cos t}\mathrm{d}t - \int_0^{\pi}\cos(nt)e^{-iw\cos t}\mathrm{d}t \\ &= \pi(J'_{n+2}(iw) - J'_n(iw)), \end{aligned} \tag{8}$$

where $\mathcal{F}$ is the Fourier transform operator and $J'_n(z)$ is the modified Bessel function of order n, i.e., $J'_n(z) = \frac{1}{\pi}\int_0^{\pi}\cos(nt)e^{-z\cos t}\mathrm{d}t$. Because $J'_n(z)$ rapidly tends to zero when the argument $|z|$ becomes less than n, $W(s)\cdot U_n(s)$ can be regarded as a high-pass filter,

$$\mathcal{F}(W(s)\cdot U_n(s))(w) \begin{cases} \approx 0, & 0 \leq w < w_{c,n}, \\ \geq 0, & w_{c,n} \leq w, \end{cases} \tag{9}$$

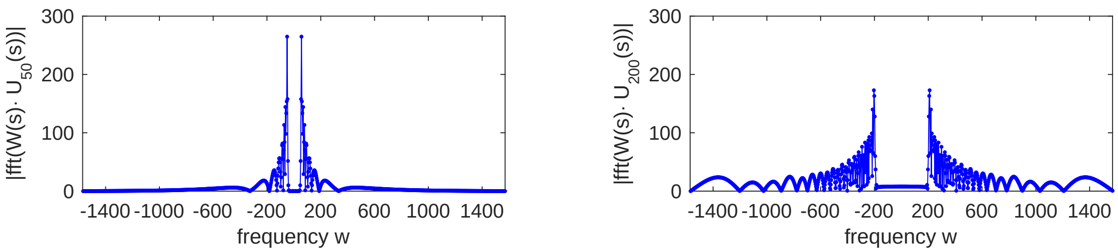

(a) $U_{50}(s) \cdot W(s)$ (b) $U_{200}(s) \cdot W(s)$

Figure 1. Discrete Fourier transforms of the Chebyshev polynomials, $U_{50}(s) \cdot W(s)$ and $U_{200}(s) \cdot W(s)$ as examples.

where $w_{c,n}$ is the cutoff frequency for order n. We approximate the cutoff frequency as $w_{c,n} \approx n$. As an illustration, the discrete fast Fourier transforms (FFT) of $W(s) \cdot U_n(s)$ for orders $n = 50$ and $n = 200$ are displayed in Fig. 1.

Therefore, the missing polynomials of orders higher than n_r only contribute to the frequency range above w_{c,n_r} and the frequency range $[0, w_{c,n_r}]$ should be complete, i.e., a circular area with radius w_{c,n_r} in the Fourier space of the object is restored correctly if we use $p_{n_r}(s, \theta)$ for reconstruction.

2.2. Regression method for sinogram restoration

In practical applications, discretization of the above formulas is necessary. We denote the projection angles as $\boldsymbol{\theta} = [\theta_0, \theta_1, \ldots, \theta_{N-1}]^\top$ where $0 \leq \theta_k < \theta_{\max}$, $k = 0, 1, ..., N-1$, $\theta_{\max}$ is the maximum scanned angle, and N is the total number of acquired projections. The available samples on each moment curve are denoted by $\boldsymbol{a}_n(\boldsymbol{\theta}) = [a_n(\theta_0), a_n(\theta_1), a_n(\theta_2), ..., a_n(\theta_{N-1})]^\top$. We seek to restore the complete 180° sinogram at angles $\boldsymbol{\theta}_{\text{comp}} = [0, 1, \ldots, (K-1)]^\top \cdot \Delta\theta$ from the acquired samples where $K = \lfloor \pi/\Delta\theta \rfloor$ and $\Delta\theta$ is the angular step.

According to HLCC and the inverse Fourier transform of Eq. (3), the moment curve $a_n(\theta)$ can also be represented as the following trigonometric Fourier series,

$$a_n(\theta) = c_{n,0} + \sum_{m=1}^{n} (c_{n,m}\cos(m\theta) + d_{n,m}\sin(m\theta)), \tag{10}$$

where $c_{n,0} = b_{n,0}$ and $(c_{n,m} - d_{n,m}i)/2 = b_{n,m}$. Accordingly, $c_{n,m} = 0$ and $d_{n,m} = 0$ when $n + m$ is odd. That is, when n is even, m can be $0, 2, 4, \ldots, n-2, n$. Thus, $a_n(\theta)$ has $n+1$ unknown coefficients denoted by $\boldsymbol{\beta}_{n,\text{e}} = [c_{n,0}, c_{n,2}, d_{n,2}, c_{n,4}, d_{n,4}, \ldots, c_{n,n}, d_{n,n}]^\top$. As a result, we get the following linear regression problem:

$$[\mathbf{1}, \cos(2\boldsymbol{\theta}), \sin(2\boldsymbol{\theta}), \cos(4\boldsymbol{\theta}), \sin(4\boldsymbol{\theta}), ..., \cos(n\boldsymbol{\theta}), \sin(n\boldsymbol{\theta})]\, \boldsymbol{\beta}_{n,\text{e}} = \boldsymbol{a}_n(\boldsymbol{\theta}), \tag{11}$$

where $\cos(\cdot)$ and $\sin(\cdot)$ are element-wise operators.

When n is odd, we get a similar regression problem with again $n+1$ unknown coefficients,

$$[\cos(\boldsymbol{\theta}), \sin(\boldsymbol{\theta}), \cos(3\boldsymbol{\theta}), \sin(3\boldsymbol{\theta}), ..., \cos(n\boldsymbol{\theta}), \sin(n\boldsymbol{\theta})]\, \boldsymbol{\beta}_{n,\text{O}} = \boldsymbol{a}_n(\boldsymbol{\theta}), \tag{12}$$

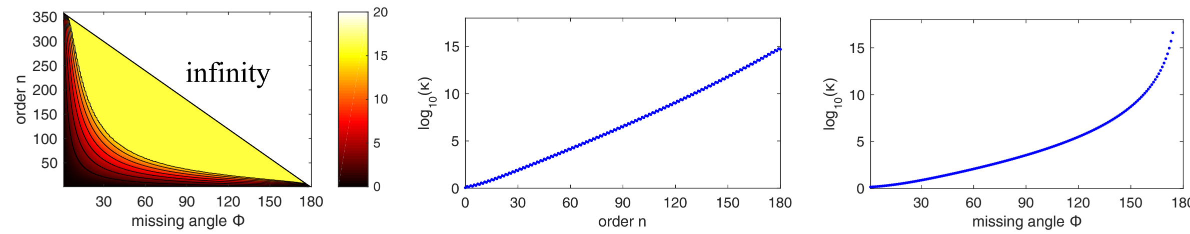

(a) Varying n and Φ (b) Varying n, $\Phi = 20°$ (c) Varying Φ, $n = 10$

Figure 2. Condition numbers of $\boldsymbol{X}_n(\boldsymbol{\theta})$ as a function of the order n and the missing angular range Φ: (a) both n and Φ vary, the condition numbers are logarithmized as $\log_{10}(\kappa_n)$ and the lines are contours with step size 2; (b) only n varies, $\Phi = 20°$, $\boldsymbol{\theta} = [0°, 0.5°, 1°, \ldots, 159.5°]^\top$; (c) only Φ varies, $n = 10$, $\boldsymbol{\theta}' = [0°, 0.5°, 1°, \ldots, 180° - \Phi]^\top$.

where $\boldsymbol{\beta}_{n,\mathrm{O}} = [c_{n,1}, d_{n,1}, c_{n,3}, d_{n,3}, \ldots, c_{n,n}, d_{n,n}]^\top$.

For each case, the above regression problems can be written as,

$$\boldsymbol{X}_n(\boldsymbol{\theta})\boldsymbol{\beta}_n = \boldsymbol{a}_n(\boldsymbol{\theta}). \tag{13}$$

With an estimate $\hat{\boldsymbol{\beta}}_n$ of the parameters $\boldsymbol{\beta}_n$, the complete nth moment curve $\hat{\boldsymbol{a}}_n(\boldsymbol{\theta}_{\text{comp}})$ is attained as

$$\hat{\boldsymbol{a}}_n(\boldsymbol{\theta}_{\text{comp}}) = \boldsymbol{X}_n(\boldsymbol{\theta}_{\text{comp}})\hat{\boldsymbol{\beta}}_n. \tag{14}$$

Then the complete sinogram can be restored using inverse Chebyshev transform (Eq. (7)) and the object can be reconstructed with any reconstruction algorithm.

The conversion of the sinogram restoration problem into the regression problem in Eq. (13) has the following benefits:

(i) $\boldsymbol{\theta}$ can be a partial angle range and it does not have to be uniformly distributed.

(ii) Computing the condition number of matrix $\boldsymbol{X}_n(\boldsymbol{\theta})$ is a practical way to analyze the ill-posedness of the sinogram restoration problem. An example is illustrated in Fig. 2. It indicates that when the order n or the missing angle $\Phi = \pi - \theta_{\max}$ increases, the condition number increases drastically. Intuitively, when n or Φ is small, the number of the unknown parameters is small and thus $\boldsymbol{\beta}_n$ can be well estimated. However, when n gets larger while Φ is fixed, the condition number κ_n increases exponentially (Fig. 2(b)). When Φ increases while n is fixed, the condition number increases even faster than exponential growth (Fig. 2(c)). Furthermore, when $n \geq N = (180° - \Phi)/\Delta\theta$, $\boldsymbol{X}_n(\boldsymbol{\theta})$ with size $N \times (n+1)$ becomes underdetermined. In these cases, the condition number tends to infinity (upper right triangle in Fig. 2(a)). Therefore, the regression problem (Eq. (13)) for sinogram restoration is ill-posed.

(iii) Various existing algorithms are available to solve the ill-posed regression problem by different solvers with different regularization terms. Louis & Törnig and Natterer solve it with the SVD pseudo-inverse or Tikhonov-Phillps regularization (Louis & Törnig 1980, Natterer 1986). It is well known that most medical images are sparse at the image gradient domain, which results in less variations on the moment curves. Therefore, the moment curves only have a few dominant frequency components.

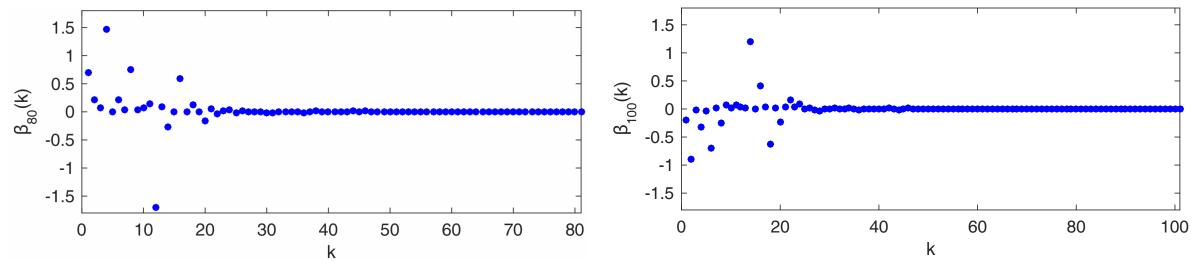

(a) $\boldsymbol{\beta}_{80}$ (b) $\boldsymbol{\beta}_{100}$

Figure 3. Sparsity of parameters, $\boldsymbol{\beta}_{80}$ and $\boldsymbol{\beta}_{100}$ of the Shepp-Logan phantom as examples.

Observing the parameters $\boldsymbol{\beta}_n$ are approximately sparse (Fig. 3), in this paper we use Lasso regression (Tibshirani 1996),

$$\boldsymbol{\beta}_n = \arg\min \frac{1}{2}||\boldsymbol{X}_n(\boldsymbol{\theta})\boldsymbol{\beta}_n - \boldsymbol{a}_n(\boldsymbol{\theta})|| + \tau_n||\boldsymbol{\beta}_n||_1, \tag{15}$$

where τ_n is a regularization coefficient. It can be solved by the iterative soft-thresholding algorithm (Daubechies et al. 2004).

2.3. Image fusion in frequency domain

The proposed regression method is applied to restore the complete sinogram $p_{n_r}(s,\theta)$. The image reconstructed from $p_{n_r}(s,\theta)$ is denoted by $f_{\text{HLCC}}(x,y)$. The reconstructed image resolution is primarily determined by the detector element size Δs; the maximum image frequency that can be resolved is $\pi/\Delta s$. Thus, we can choose $n_r \approx \pi/\Delta s$ to restore an adequate discrete sinogram. If the number of orders n_r is not large enough, the reconstructed image will suffer from ringing artifacts. However, as aforementioned, the condition number of $\boldsymbol{X}_n(\boldsymbol{\theta})$ increases drastically when n increases. Therefore, only certain orders of the moment curves are estimated correctly. Let n_c denote the highest order that is still estimated correctly. Then, the frequency components of $f_{\text{HLCC}}(x,y)$ are only correct inside a circular area with radius $w = w_{c,n_c}$. As a consequence, regression errors in the restored moment curves from order n_c+1 to n_r will introduce artifacts. Since it is difficult to find a compromise between these artifacts and ringing artifacts by selecting an optimal n_r, we opt to choose a relatively large n_r to avoid ringing artifacts, followed by a bilateral filtering (BF) and an image fusion to mitigate regression artifacts.

We denote the image reconstructed from the limited angle sinogram by $f_{\text{limited}}(x,y)$ and its 2-D Fourier transform in polar coordinates by $F_{\text{limited}}(w,\theta)$. The central slice theorem reveals that a double wedge region is missing in $F_{\text{limited}}(x,y)$, i.e.,

$$F_{\text{limited}}(w,\theta)|_{\theta_{\max}\le\theta<\pi,-\infty<w<\infty} = 0. \tag{16}$$

We only want to use the restored information contained in f_{HLCC} to fill in this unobserved region. For this purpose, we design a double wedge-shaped mask $M(w,\theta)$ in frequency domain where values outside the double wedge zero region are 1. The binary mask $M(w,\theta)$ is smoothed by a Gaussian filter to get a smooth transition at its

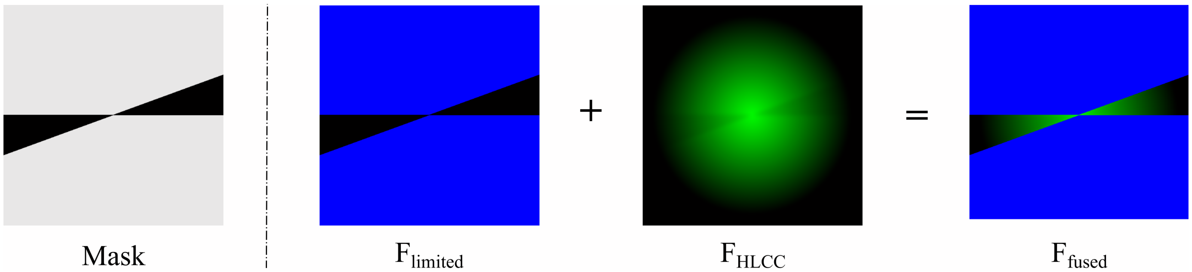

Figure 4. Illustration of the image fusion at the frequency domain using the mask, the black, blue, and green areas are the missing, measured, and HLCC estimated frequency components, respectively, where the faded green area might be not correctly estimated.

boundaries. A small region around the origin is exempt from this smoothing. Then the following image fusion (Fig. 4) is performed,

$$F_{\text{fused}}(w,\theta) = F_{\text{limited}}(w,\theta)\cdot M(w,\theta) + F_{\text{HLCC}}(w,\theta)\cdot(1-M(w,\theta)), \qquad (17)$$

where F_{HLCC} is the 2-D Fourier transform of f_{HLCC}. The fused image f_{fused} can be obtained with a 2-D inverse Fourier transform of F_{fused}.

Thereby, the measured frequency components are fully used. However, higher frequency components inside the double wedge region are still missing or erroneously estimated. Thus, bilateral filtering can be applied to f_{HLCC} before the fusion to obtain only the most prominent and reliable high frequency components associated with sharp edges and suppress erroneous ones (Tomasi & Manduchi 1998). It is defined as,

$$f_{\text{BF}}(\boldsymbol{x}) = \frac{\sum_{\boldsymbol{x}'\in\mathcal{N}} f_{\text{HLCC}}(\boldsymbol{x}')\cdot c(\boldsymbol{x},\boldsymbol{x}')\cdot s(f_{\text{HLCC}}(\boldsymbol{x}), f_{\text{HLCC}}(\boldsymbol{x}'))}{\sum_{\boldsymbol{x}'\in\mathcal{N}} c(\boldsymbol{x},\boldsymbol{x}')\cdot s(f_{\text{HLCC}}(\boldsymbol{x}), f_{\text{HLCC}}(\boldsymbol{x}'))}, \qquad (18)$$

where $\boldsymbol{x}$ is the pixel index, $\mathcal{N}$ denotes the neighborhood of pixel $\boldsymbol{x}$, and Gaussian functions $c(\boldsymbol{x},\boldsymbol{x}')$ and $s(v,v')$ measure the spatial closeness and range similarity with standard deviations σ_c and σ_s,

$$c(\boldsymbol{x},\boldsymbol{x}') = e^{-||\boldsymbol{x}-\boldsymbol{x}'||_2^2/\sigma_c^2}, \qquad s(v,v') = e^{-|v-v'|^2/\sigma_s^2}. \qquad (19)$$

In Eq. (17), we replace F_{HLCC} by F_{BF} which is the Fourier transform of f_{BF}. Then, another fused frequency domain estimate F_{fused2} and corresponding image f_{fused2} are obtained.

2.4. Experiments

To evaluate the performance of our proposed method, three experiments on the standard high-contrast Shepp-Logan phantom (Fig. 7(a)) are conducted. The size of the Shepp-Logan phantom is 204.8 mm × 204.8 mm. The linear attenuation coefficients are between [0, 0.08]/mm. We convert it to Hounsfield scale between [-1000, 3000] HU. For the first experiment, a limited angle sinogram is computed analytically (Toft & Sørensen 1996) in a parallel-beam trajectory. The total scanned angular range is 160° and the angular step is 0.5°. The number of the equal-space detector pixels is 1537 and the detector element size is 0.2 mm, which is kept the same for other experiments. For the first experiment, we do not add artificial noise. For the second experiment, we additionally simulate Poisson noise during acquisition. We assume that each X-ray contains $I_0 = 10^4$ photons. After passing through the object the number of photons for each X-ray is $I(s,\theta) = I_0 e^{-p(s,\theta)}$. Poisson noise is simulated as $I'(s,\theta) = \mathcal{P}(I(s,\theta))$, where $\mathcal{P}(\lambda)$ is a Poisson random variable with a mean parameter λ. Thus, the sinogram with Poisson noise is $p'(s,\theta) = -\ln(I'/I_0)$. For the third experiment, we choose smaller angular ranges. Two limited angle sinograms are analytically computed without Poisson noise in 140° and 120° trajectories.

For comparison, Ridge regression (Tikhonov 1943) is performed for the noise-free Shepp-Logan phantom, i.e., $\boldsymbol{\beta}_n = \arg\min \frac{1}{2}||\boldsymbol{X}_n(\boldsymbol{\theta})\boldsymbol{\beta}_n - \boldsymbol{a}_n(\boldsymbol{\theta})|| + \tau_n||\boldsymbol{\beta}_n||_2$, where the values of τ_n are chosen the same as those in Lasso regression. An extrapolation/interpolation method based on the Gerchberg-Papoulis algorithm is also performed for the noise-free Shepp-Logan phantom. The Fourier property of the sinogram (Edholm et al. 1986, Mazin & Pelc 2010) indicates that the sinogram is band-limited. Therefore, we apply a double-wedge filter instead of a typical low-pass filter at the Fourier domain of the sinogram as shown in (Pohlmann et al. 2014).

As a preliminary study for clinical data, we take one slice reconstructed from a 3-D clinical head dataset as a ground truth image (Figs. 12(a) and 12(g)). The dataset is acquired from a Siemens Artis zee angiographic C-arm system (Siemens Healthcare GmbH, Forchheim, Germany). The image size of the chosen slice is 512×512 with an isotropic pixel size of 0.4 mm. The linear attenuation coefficients are between [-1000, 2000] HU. A limited angle sinogram is simulated using a ray-driven method with a sampling rate of 7.5/mm in the 160° parallel-beam trajectory.

Empirically, we choose $n_r = 720$ to restore the sinograms. For each order, the soft-threshold $\tau_n = 0.001 \cdot (1 - n/1000)$ is used for Lasso regression in Eq. (15) and the iteration stops when $||\hat{\boldsymbol{\beta}}_n^{l+1} - \hat{\boldsymbol{\beta}}_n^{l}||_2/||\hat{\boldsymbol{\beta}}_n^{l}||_2 < 10^{-4}$ where $\hat{\boldsymbol{\beta}}_n^{l}$ are the estimated parameters at the l-th iteration. We use the linear correlation coefficient of the estimated moment curve and the ground truth moment curve to indicate the accuracy of the estimated parameters $\hat{\boldsymbol{\beta}}_n$, i.e.,

$$r_n = \sum_{k=N}^{K-1} (a_n(\theta_k) - \mu)(\hat{a}_n(\theta_k) - \hat{\mu})/(\sigma \cdot \hat{\sigma}), \tag{20}$$

where μ and σ are the mean and standard deviation of the ground truth moment curve at the missing region, $\hat{\mu}$ and $\hat{\sigma}$ are the mean and standard deviation of $\hat{\boldsymbol{a}}_n(\boldsymbol{\theta}_{\text{comp}})$ at the missing part, and $\hat{a}_n(\theta_k)$ is the k-th element of $\hat{\boldsymbol{a}}_n(\boldsymbol{\theta}_{\text{comp}})$.

The images are reconstructed using FBP with the Ram-Lak filter. The size of the reconstructed images is 512×512 with an isotropic pixel size of 0.4 mm. The bilateral filter is characterized by $\sigma_c = 30$, $\sigma_s = 0.05$, and an $\mathcal{N} = 40 \times 40$ neighborhood. The binary mask $M(w,\theta)$ is smoothed by a Gaussian filter with a cutoff frequency at 0.4 Nyquist frequency. The experimental setup is implemented in CONRAD (Maier et al. 2013), a software framework for medical imaging processing.

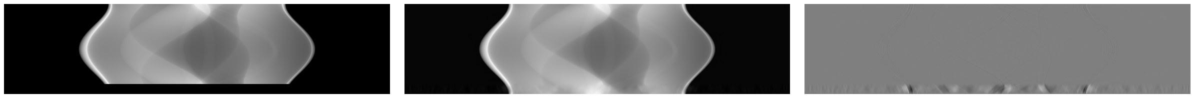

(a) Limited angle sinogram, 160° (b) Restored sinogram, 180° (c) Restoration error

Figure 5. The measured limited angle sinogram, the restored complete sinogram, and the difference of restored sinogram and ground truth of the Shepp-Logan phantom, noise free, window for (a) and (b): [0, 4], window for (c): [-1, 1].

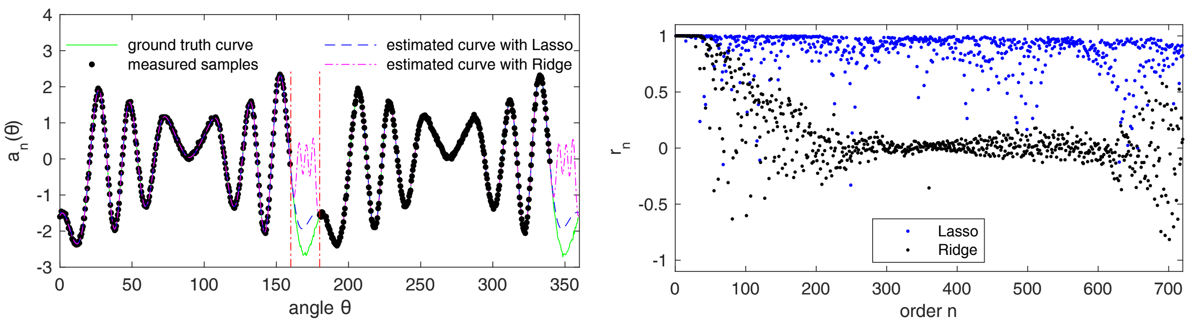

(a) Moment curve fitting, $n = 100$ (b) Linear correlation coefficients

Figure 6. Lasso regression and Ridge regression results of the Shepp-Logan phantom, noise-free: (a) Plot of curve $\hat{\boldsymbol{a}}_{100}(\boldsymbol{\theta}_{\mathrm{comp}})$ as an example. The area in the two red lines corresponds to the missing region. The angular range $[180°, 360°)$ is obtained from $p(s, \theta) = p(-s, \theta + \pi)$. The linear correlation coefficient between the green and blue curves is 0.95 while it is -0.6 between the green and magenta curves. (b) Linear correlation coefficients of the estimated curve and the ground truth curve at the missing region for different orders.

3. Results

The 160° limited angle sinogram, the restored sinogram using Lasso regression, and the difference between the restored sinogram and the 180° ground truth sinogram of the noise-free Shepp-Logan phantom are shown in Fig. 5. From the simulated sinogram, the partial moment curves $\boldsymbol{a}_n(\boldsymbol{\theta})$ are computed and the complete moment curves $\hat{\boldsymbol{a}}_n(\boldsymbol{\theta}_{\mathrm{comp}})$ are estimated with Lasso regression. The curves of $\hat{\boldsymbol{a}}_{100}(\boldsymbol{\theta}_{\mathrm{comp}})$ using Lasso regression and Ridge regression are plotted in Fig. 6(a) as an example to illustrate the regression problem. It shows that both estimated moment curves have some deviations to the ground truth moment curve $\boldsymbol{a}_{100}(\boldsymbol{\theta}_{\mathrm{comp}})$, indicating the existence of regression errors. However, the curve estimated by Lasso is closer to the ground truth curve. The linear correlation coefficients for different orders are plotted in Fig. 6(b), which reveals that only low orders of the moment curves, particularly when n is smaller than 40, can be recovered perfectly. When the orders are higher than 40, outliers occur for both regression algorithms. Compared with Ridge regression, Lasso regression achieves significantly better correlations, especially in higher orders.

The reconstructed images, their absolute differences from the ground truth, and their Fourier transforms for the noise-free Shepp-Logan phantom using Lasso regression

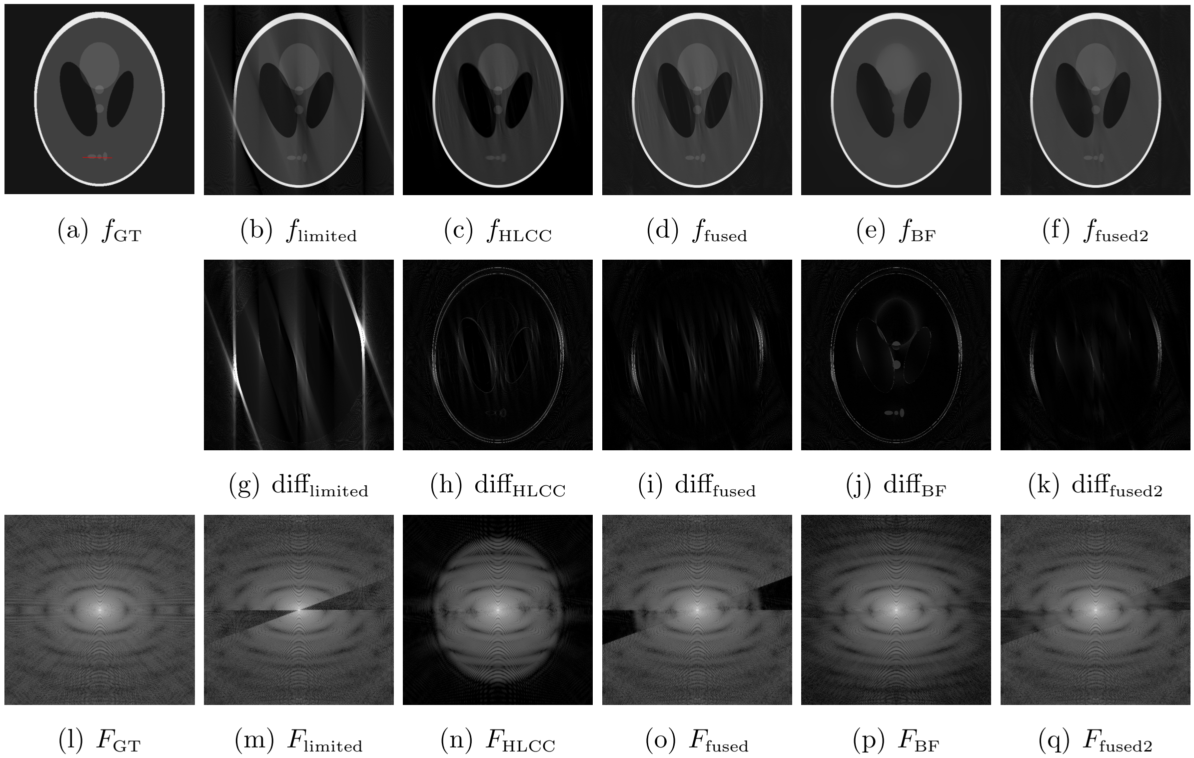

Figure 7. Reconstructions of the Shepp-Logan phantom and their Fourier transforms, noise-free. The RMSEs for f_{limited}, f_{HLCC}, f_{fused}, f_{BF}, and f_{fused2} are 302 HU, 131 HU, 91 HU, 118 HU, and 78 HU, respectively. Window: [-1400, 3400] HU and [-1000, 1000] HU for the top row and the middle row, respectively. The frequency amplitudes are logarithmized and all displayed in the same window.

are shown in Fig. 7. Comparing f_{HLCC} with f_{limited}, large streak artifacts are reduced and the shape of the outer boundary is reconstructed better in f_{HLCC}. However, it suffers from artifacts caused by regression errors, which appear as small streaks. Fig. 7(h) displays that the edges in f_{HLCC} also have large errors. It is apparent that a double wedge region is missing in F_{limited} while high frequency components are lost in F_{HLCC} due to the low number of n_r. The fused frequency components are shown in Fig. 7(o) where the high frequency components inside the double wedge region are still missing or erroneous. Correspondingly, artifacts still exist in f_{fused} and the outer boundary has large errors at the left and right sides. However, the edges at the upper and lower areas are sharper because they correspond to the measured frequency area due to their spatial orientations. The edge sharpness improvement can be appreciated in the difference image Fig. 7(i) and the line profiles plotted in Fig. 8. Figs. 7(e) and 7(p) demonstrate that the bilateral filter can remove artifacts caused by regression errors and partially recover high frequency components. With the image fusion, streak artifacts are reduced in f_{fused2} while avoiding the introduction of new artifacts due to regression. The root-mean-square error (RMSE) is reduced from 302 HU to 78 HU.

For comparison, the reconstructed images f_{HLCC} and f_{fused2} using Ridge regression are shown in Figs. 9(a) and (b). Even though some streaks are reduced, the outer

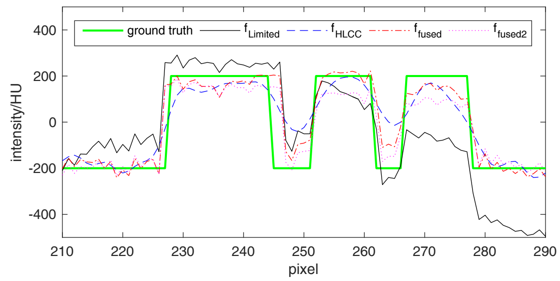

Figure 8. Line profiles of different reconstructions of the noise-free Shepp-Logan phantom. The location of the plotted line is shown in Fig. 7(a).

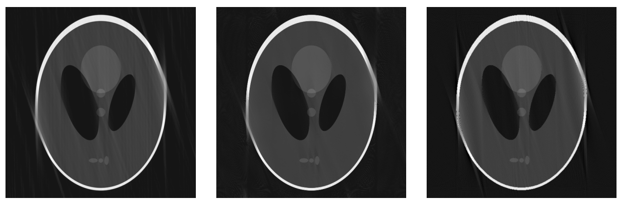

(a) f_{HLCC}, Ridge (b) f_{fused2}, Ridge (c) $f_{\text{G-P}}$

Figure 9. Reconstructions of the noise-free Shepp-Logan phantom with Ridge regression and the Gerchberg-Papoulis based extrapolation/interpolation algorithm. The RMSEs for f_{HLCC} (Ridge), f_{fused2} (Ridge), and $f_{\text{G-P}}$ are 208 HU, 181 HU, and 179 HU, respectively. Window: [-1400, 3400] HU.

boundaries of the Shepp-Logan phantom are not well reconstructed, which demonstrates the advantage of Lasso regression over Ridge regression. The reconstruction result of the Gerchberg-Papoulis based extrapolation/interpolation algorithm is also displayed in Fig. 9(c), denoted by $f_{\text{G-P}}$. Like Figs. 9(a) and (b), the outer boundaries in $f_{\text{G-P}}$ are not well reconstructed either.

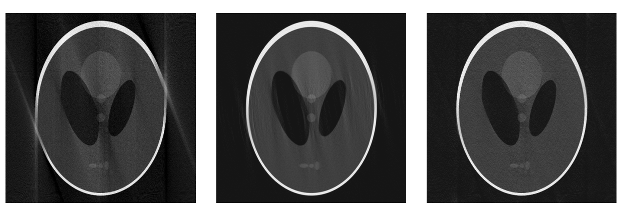

(a) f_{limited} (b) f_{HLCC} (c) f_{fused2}

Figure 10. Reconstructions of the Shepp-Logan phantom with Poisson noise. The RMSEs are 355 HU, 135 HU, and 175 HU, respectively. Window: [-1400, 3400] HU.

The reconstructions of f_{limited}, f_{HLCC}, and f_{fused2} with Poisson noise are displayed in Fig. 10. Fig. 10(b) indicates that Poisson noise is suppressed at f_{HLCC}. The results demonstrate that our proposed method also works in a noisy situation.

The reconstruction results of the noise-free Shepp-Logan phantom in 140° and 120° angular ranges are shown in Fig. 11. With more data missing, more artifacts are caused by regression errors and thus the image quality degrades. However, our method is still

(a) $f_{\text{limited}}, 140°$ (b) $f_{\text{HLCC}}, 140°$ (c) $f_{\text{fused2}}, 140°$ (d) $f_{\text{limited}}, 120°$ (e) $f_{\text{HLCC}}, 120°$ (f) $f_{\text{fused2}}, 120°$

Figure 11. Reconstruction results of the noise-free Shepp-Logan phantom in the angular range of 140° and 120°. The RMSEs from left to right are 435 HU, 194 HU, 160 HU, 532 HU, 309 HU, and 287 HU, respectively. Window: [-1400, 3400] HU.

able to roughly restore the shape of the outer boundaries.

The results of the preliminary clinical experiments are shown in Fig. 12. Comparing Fig. 12(f) with Fig. 12(b), f_{fused2} offers a better bone outline. In the narrower window, the brain textures in f_{fused2} (Fig. 12(l)) can be better distinguished. In contrast, they are obscured by streak artifacts or artifacts caused by the regression in Figs. 12(h) and 12(i). The intensity offset in f_{limited} due to the missing data is corrected in f_{fused2}.

4. Discussion

With the regression, an approximate sinogram can be restored. Since our regression formulation integrates HLCC, the estimated moment curves are smooth even though they are partially inaccurate at the missing region (Fig. 6(a)). As a result, the restored sinogram is continuous over the whole angular range of $[0, \pi)$. Due to ill-posedness of the problem, high order moment curves are difficult to estimate (Fig. 6(b)). Consequently, the restored sinogram has errors at the missing angular range (Fig. 5(c)).

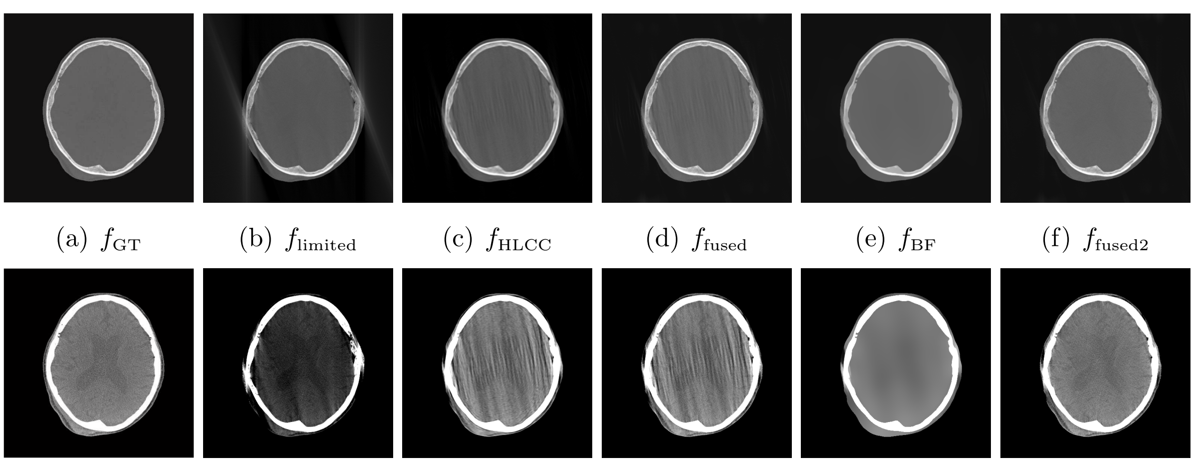

(a) f_{GT} (b) f_{limited} (c) f_{HLCC} (d) f_{fused} (e) f_{BF} (f) f_{fused2}

(g) f_{GT} (h) f_{limited} (i) f_{HLCC} (j) f_{fused} (k) f_{BF} (l) f_{fused2}

Figure 12. Preliminary results of clinical data, the RMSEs for f_{limited}, f_{HLCC}, f_{fused}, f_{BF}, and f_{fused2} are 187 HU, 73 HU, 62 HU, 72 HU, and 56 HU, respectively. Window: [-1200, 2000] HU and [-200, 300] HU for top and bottom images, respectively.

The image quality of f_{HLCC} is highly dependent on the accuracy of the regression estimation. On the one hand, high order moment curves are required to achieve a proper spatial resolution. On the other hand, as aforementioned, the ill-posedness prohibits their correct recovery. In this paper, we propose to utilize Lasso regression, which exploits sparsity at the domain of Fourier coefficients of the moment curves. Compared with Ridge regression (Fig. 6(b)), Lasso regression can estimate higher order moment curves better, which contribute to the image quality, especially to high contrast structures. However, some orders still show errors when using Lasso regression. Thus, artifacts exist in f_{HLCC} (Figs. 7(c) and 12(i)). To reduce these artifacts, one potential approach is to explore a more effective regression algorithm with other regularization terms. In this paper, two simple but effective techniques are applied:

(i) A bilateral filter is used to reduce these artifacts and partially recover some high frequency components. Even though some high frequency components might be incorrect, the most prominent and reliable ones are recovered which are associated with dominant high contrast edges and thus crucial for image quality. However, the fine structures like small ellipses and the brain textures in Figs. 7(e) and 12(k) are removed by the bilateral filter. Hence, using bilateral filter alone is not sufficient to obtain a high quality image and an additional fusion operation is necessary.

(ii) A mask is designed for fusion in frequency domain. With this mask, the frequency components inside the double wedge region are taken from the restored sinogram while the measured frequency components outside the double wedge region are preserved. The fusion along with the bilateral filtering can reduce artifacts efficiently while preserving fine structures (Figs. 7(k) and 12(f)). Since the zero frequency component is taken from f_{HLCC}, the intensity offset in f_{limited} is also corrected in the fused images.

Our proposed method is robust to Poisson noise. Noise mostly adds high frequency components to moment curves. In the regression step, Lasso regression will estimate smooth moment curves according to HLCC. Hence, the high frequency noise will be reduced. Therefore, noise is somewhat suppressed in f_{HLCC}. However, it is brought back at the fusion step by reintroducing the acquired frequency components.

Louis and Natterer pointed out that the extrapolation/interpolation procedure for sinogram restoration is as fast as FBP (Louis & Natterer 1983, Louis & Törnig 1980, Louis 1981). Our method uses the iterative soft-thresholding algorithm to solve Eq. (13), which is a series of smaller problems with only $n+1$ unknown parameters for each order n and can be solved efficiently. Additionally, we utilize a bilateral filter and 2-D FFT for fusion in frequency domain. While bilateral filtering does introduce an additional computational cost, our method is still faster than iterative algorithms with TV regularization. Quinto extrapolated the limited angle sinogram using linear interpolation along the angular direction in order to apply their adapted Lambda Tomography algorithm called exterior reconstruction algorithm (ERA) (Quinto 1998). However, ERA requires *a priori* information about the shape of the object, specifically an annulus object with known radius, while our method does not.

5. Conclusion

In this paper, we propose a regression and fusion method to restore the missing data in limited angle tomography. The limited angle sinogram restoration problem is converted to a regression problem based on HLCC. By computing the SVD of the regression matrix $\boldsymbol{X}_n(\boldsymbol{\theta})$, its ill-posedness is investigated. To solve the regression problem, Lasso regression is chosen. However, it is only able to estimate the low order moment curves accurately. Correspondingly, only low frequency components of the imaged object are estimated correctly. Therefore, bilateral filtering is utilized to obtain the most prominent and reliable higher frequency components and suppress erroneous ones. Afterwards, a fusion is performed in the frequency domain. The frequency components at the missing double wedge region are attained from the restored ones while the original measured frequency components are preserved. With our proposed method, the intensity offset is compensated and streak artifacts are reduced in the final fused image.

Disclaimer: The concepts and information presented in this paper are based on research and are not commercially available.

6. References

Aichert A, Berger M, Wang J, Maass N, Doerfler A, Hornegger J & Maier A 2015 Epipolar consistency in transmission imaging *IEEE Transactions on Medical Imaging* **34**(10), 1–15.

Chen Z, Jin X, Li L & Wang G 2013 A limited-angle CT reconstruction method based on anisotropic TV minimization *Physics in Medicine and Biology* **58**(7), 2119.

Clackdoyle R & Desbat L 2015 Data consistency conditions for truncated fanbeam and parallel projections *Medical Physics* **42**(2), 831–845.

Constantino E & Ozanyan K B 2008 Sinogram recovery for sparse angle tomography using a sinusoidal hough transform *Measurement Science and Technology* **19**(9), 094015.

Daubechies I, Defrise M & De Mol C 2004 An iterative thresholding algorithm for linear inverse problems with a sparsity constraint *Communications on pure and applied mathematics* **57**(11), 1413–1457.

Davison M E 1983 The ill-conditioned nature of the limited angle tomography problem *SIAM Journal on Applied Mathematics* **43**(2), 428–448.

Deans S R 2007 *The Radon transform and some of its applications* Courier Corporation.

Debbeler C, Maass N, Elter M, Dennerlein F & Buzug T M 2013 A new CT rawdata redundancy measure applied to automated misalignment correction *in* 'Proceedings of the 12th international meeting on fully three-dimensional image reconstruction in radiology and nuclear medicine, edited by Richard Leahy and Jinyi Qi' pp. 264–267.

Edholm P R, Lewitt R M & Lindholm B 1986 Novel properties of the fourier decomposition of the sinogram *in* 'Physics and Engineering of Computerized Multidimensional Imaging and Processing' International Society for Optics and Photonics pp. 8–18.

Frikel J 2013 Sparse regularization in limited angle tomography *Applied and Computational Harmonic Analysis* **34**(1), 117–141.

Hanson K M & Wecksung G W 1983 Bayesian approach to limited-angle reconstruction in computed tomography *JOSA* **73**(11), 1501–1509.

Happonen A & Ruotsalainen U 2005 A comparative study of angular extrapolation in sinogram and stackgram domains for limited angle tomography *Image Analysis* pp. 263–347.

Helgason S 1980 *The Radon transform* Boston, MA: Birkhauser.

Hsieh J, Chao E, Thibault J, Grekowicz B, Horst A, McOlash S & Myers T 2004 A novel reconstruction algorithm to extend the ct scan field-of-view *Medical physics* **31**(9), 2385–2391.

Huang Y, Taubmann O, Huang X, Haase V, Lauritsch G & Maier A 2016 A new weighted anisotropic total variation algorithm for limited angle tomography *in* 'the 2016 IEEE International Symposium on Biomedical Imaging: From Nano to Macro' pp. 585–588.

Kudo H & Saito T 1991 Sinogram recovery with the method of convex projections for limited-data reconstruction in computed tomography *Journal of the Optical Society of America A* **8**(7), 1148–1160.

Lewitt R M 1983 Reconstruction algorithms: transform methods *Proceedings of the IEEE* **71**(3), 390–408.

Louis A K 1981 Approximation of the radon transform from samples in limited range *in* 'Mathematical Aspects of Computerized Tomography' Springer pp. 127–139.

Louis A K 1986 Incomplete data problems in X-ray computerized tomography: I. singular value decomposition of the limited angle transform *Numerische Mathematik* **48**(3), 251–262.

Louis A K & Natterer F 1983 Mathematical problems of computerized tomography *Proceedings of the IEEE* **71**(3), 379–389.

Louis A K & Törnig W 1980 Picture reconstruction from projections in restricted range *Mathematical Methods in the Applied Sciences* **2**(2), 209–220.

Ludwig D 1966 The radon transform on euclidean space *Communications on Pure and Applied Mathematics* **19**(1), 49–81.

Maier A, Hofmann H, Berger M, Fischer P, Schwemmer C, Wu H, Müller K, Hornegger J, Choi J, Riess C, Keil A & Fahrig R 2013 CONRAD - a software framework for cone-beam imaging in radiology *Medical Physics* **40**(11), 111914.

Mazin S R & Pelc N J 2010 Fourier properties of the fan-beam sinogram *Medical Physics* **37**(4), 1674–1680.

Natterer F 1986 *The mathematics of computerized tomography* Vol. 32 Society for Industrial and Applied Mathematics.

Olson T 1995 Stabilized inversion for limited angle tomography *IEEE Engineering in Medicine and Biology Magazine* **14**(5), 612–620.

Patch S 2001 Moment conditions indirectly improve image quality *Contemporary Mathematics* **278**, 193–206.

Patch S K 2002 Consistency conditions upon 3D CT data and the wave equation *Physics in medicine and biology* **47**(15), 2637.

Pohlmann M, Berger M, Maier A, Hornegger J & Fahrig R 2014 Estimation of missing fan-beam projections using frequency consistency conditions *in* 'Proceedings of the third international conference on image formation in x-ray computed tomography' pp. 203–207.

Qu G r & Jiang M 2009 Landweber iterative methods for angle-limited image reconstruction *Acta Mathematicae Applicatae Sinica (English Series)* **25**(2), 327–334.

Qu G r, Lan Y s & Jiang M 2008 An iterative algorithm for angle-limited three-dimensional image reconstruction *Acta Mathematicae Applicatae Sinica (English Series)* **24**(1), 157–166.

Quinto E T 1998 Exterior and limited-angle tomography in non-destructive evaluation *Inverse Problems* **14**(2), 339.

Quinto E T 2006 An introduction to X-ray tomography and radon transforms *in* 'Proceedings of symposia in Applied Mathematics' Vol. 63 p. 1.

Quinto E T 2007 Local algorithms in exterior tomography *Journal of computational and applied mathematics* **199**(1), 141–148.

Riess C, Berger M, Wu H, Manhart M, Fahrig R & Maier A 2013 TV or not TV? That is the Question *in* 'Fully 3D Image Reconstruction in Radiology and Nuclear Medicine' pp. 341–344.

Ritschl L, Bergner F, Fleischmann C & Kachelrieß M 2011 Improved total variation-based CT image reconstruction applied to clinical data *Physics in Medicine and Biology* **56**(6), 1545.

Saito T & Kudo H 1988 High quality CT image reconstruction from a small number of projections *in* 'Acoustics, Speech, and Signal Processing, 1988. ICASSP-88., 1988 International Conference on' IEEE pp. 1272–1275.

Sidky E Y & Pan X 2008 Image reconstruction in circular cone-beam computed tomography by constrained, total-variation minimization *Physics in Medicine and Biology* **53**(17), 4777.

Siltanen S, Kolehmainen V, Järvenpää S, Kaipio J, Koistinen P, Lassas M, Pirttilä J & Somersalo E 2003 Statistical inversion for medical x-ray tomography with few radiographs: I. general theory *Physics in Medicine and Biology* **48**(10), 1437.

Tibshirani R 1996 Regression shrinkage and selection via the lasso *Journal of the Royal Statistical Society. Series B (Methodological)* pp. 267–288.

Tikhonov A N 1943 On the stability of inverse problems *in* 'Doklady Akademii Nauk SSSR' Vol. 39 pp. 195–198.

Toft P A & Sørensen J A 1996 The Radon transform-theory and implementation PhD thesis Technical University of DenmarkDanmarks Tekniske Universitet, Department of Informatics and Mathematical ModelingInstitut for Informatik og Matematisk Modellering.

Tomasi C & Manduchi R 1998 Bilateral filtering for gray and color images *in* 'Computer Vision, 1998. Sixth International Conference on' IEEE pp. 839–846.

Willsky A S & Prince J L 1990 Constrained sinogram restoration for limited-angle tomography *Optical Engineering* **29**(5), 535–544.

Wu H, Maier A, Fahrig R & Hornegger J 2012 Spatial-temporal Total Variation Regularization (STTVR) for 4D-CT Reconstruction *in* 'Proceedings of SPIE Medical Imaging 2012'.

Würfl T, Ghesu F C, Christlein V & Maier A 2016 Deep Learning Computed Tomography *in* 'Medical Image Computing and Computer-Assisted Intervention MICCAI 2016' Vol. 3 pp. 432–440.

Xia Y, Bauer S, Maier A, Berger M & Hornegger J 2015 Patient-bounded extrapolation using low-dose priors for volume-of-interest imaging in C-arm CT *Medical Physics* **42**(4), 1787–1796.

Zamyatin A A & Nakanishi S 2006 Sinogram correction methods using sinogram decomposition *in* 'Nuclear Science Symposium Conference Record, 2006. IEEE' Vol. 6 IEEE pp. 3438–3440.

Zhang H, Li L, Qiao K, Wang L, Yan B, Li L & Hu G 2016 Image prediction for limited-angle tomography via deep learning with convolutional neural network *arXiv preprint arXiv:1607.08707* .